Zircon-to-reidite phase transition enhanced by minor radiation damage: Implications for hypervelocity impacts

Shuai Nan [a,b,§,†] and Sisi Wang [a,c,†], Fuxiang Zhang [d], Jingjing Niu [a], Pengfei Zhai [e], Yingxin Liu [c], Lynn A. Boatner [f,‡], Shan Qin [g], Jie Liu [e], Maik Lang [h], Rodney C. Ewing [i,*], and Weixing Li [a,*]

[a] State Key Laboratory of Tibetan Plateau Earth System Science, Institute of Tibetan Plateau Research, Chinese Academy of Sciences, Beijing 100101, China

[b] University of Chinese Academy of Sciences, Beijing 100049, China

[c] School of Gemology, China University of Geosciences, Beijing 100083, China

[d] Songshan Lake Materials Laboratory, Dongguan, Guangdong 523808, China

[e] Institute of Modern Physics, Chinese Academy of Sciences, Lanzhou, Gansu 730000, China

[f] Materials Science & Technology Division, Oak Ridge National Laboratory, P.O. Box 2008, Oak Ridge, TN 37831-6044, USA

[g] School of Earth and Space Sciences, Peking University, Beijing 100871, China

[h] Department of Nuclear Engineering, University of Tennessee, Knoxville, TN 37996, USA

[i] Department of Earth & Planetary Sciences, Stanford University, Stanford, CA 94305-2115, USA

[†]Equal contribution. [‡]Retired. [§]Present address: Songshan Lake Materials Laboratory, Dongguan, Guangdong 523808, China.

[*]Corresponding author: wxli@itpcas.ac.cn or rewing1@stanford.edu

Abstract

Reidite, a high-pressure phase of zircon, is increasingly identified at terrestrial impact sites. Despite its growing recognition, the potential applications for estimating minimum impact pressure face impediments due to existing discrepancies in the condition of zircon-reidite transformation, controversial models governing the transformation mechanism, and unclear effects of pre-existing radiation damage on reidite formation. Here, we show enhanced reidite formation by synchrotron X-ray diffraction, Raman spectroscopy, and transmission electron microscopy analyses of zircon grains that have experienced different alpha-decay doses from U and Th impurities and subsequent pressurization in diamond anvil cells. Below ~1×10^{18} α-decay events/g, the α-decay-induced isolated point defects in the still crystalline zircon facilitate the minor atomic readjustments required for reidite formation. However, above this dose, the loss of long-range periodicity in severely damaged or even metamict zircon inhibits the transformation. The enhanced reidite formation by minor radiation damage coincides with the more common occurrence of reidite at impact sites for which the precursor zircon has a relatively lower alpha-decay-event dose before the impact event. In addition, the detailed atomic-scale structures of twinned reidite provide unambiguous evidence for a characteristic internal stress-induced martensitic transition. These findings have important implications for interpreting the formation conditions of natural reidite due to the convergence of pressure from the static, shockwave, and natural reidite samples.

Keywords: radiation damage; zircon; hypervelocity impacts; high pressure, Raman, Synchrotron X-ray diffraction

1 Introduction

The only preserved examples of natural reidite ($ZrSiO_4$, $I4_1/a$) are transformed from hypervelocity metamorphosed zircon ($ZrSiO_4$, $I4_1/amd$) (Glass and Liu, 2001; Glass *et al.*, 2002). Out of ~200 reported impact structures (Schmieder and Kring, 2020), reidite has been found at only 15 sites (Erickson *et al.*, 2017; Cavosie *et al.*, 2021). Still, reidite is a pressure indicator for shockwave pressures over ~20 GPa (Cavosie *et al.*, 2021). In the laboratory, the synthesis of reidite can be achieved through either the shockwave method, which involves the rapid compression of a sample through impact or explosive means (Kusaba *et al.*, 1985; Fiske *et al.*, 1994; Erickson *et al.*, 2020a; Christoffersen *et al.*, 2023), or the diamond anvil cell (DAC) method, by which a sample is compressed between the tips of two opposing diamond anvils (van Westrenen *et al.*, 2004; Mihailova *et al.*, 2019; Nan *et al.*, 2022). These experiments play a vital role in elucidating the still-controversial formation mechanism and conditions of natural reidite (Kusaba et al., 1985; Leroux et al., 1999; Montalvo et al., 2019). Thus, zircon and reidite have attracted considerable interest in geoscience, high-pressure minerals, and materials science (Ono *et al.*, 2004; Glasmacher *et al.*, 2006; Yue *et al.*, 2016; Timms *et al.*, 2017; Cox *et al.*, 2018; Erickson *et al.*, 2020b). Of particular significance is how to constrain the conditions of reidite formation, which requires addressing the three crucial problems below.

Firstly, the DAC method can constrain the reidite formation uniquely despite its differences in timescale and environment with other methods or approaches. Although the DAC method has a much longer pressurization time than the shockwave and naturally occurring samples, the *in situ* static DAC method allows continuous measurements of the reidite fraction by changing the pressure applied on a single sample. In contrast, one cannot practically monitor the dynamic process of reidite growth for shocked or natural samples as a function of pressure due to the short pressurization time. Despite the

different pressurization timescales and environments, the data converge at ~20 GPa for the critical transition pressure to start the transition and at ~40 GPa for the completion pressure to fully complete the transition from the three separate sources, *i.e.*, the static experiments (van Westrenen *et al.*, 2004), natural reidite samples (Cavosie *et al.*, 2021; Wittmann *et al.*, 2021) and shockwave experiments (Fiske *et al.*, 1994), suggesting a similar mechanism governing the transition. In addition, first principle calculations show a significantly lower critical transition pressure (~5-12 GPa) than that (~20 GPa) measured by the DAC method in zircon (Du *et al.*, 2012; Mihailova *et al.*, 2019; Nan *et al.*, 2022). By considering the contribution of the zircon-scheelite transition process in zircon-structured hafnon, recent phonon dispersion calculations show that the critical transition pressure converges between the phonon dispersion calculations (~22.1 GPa) and the DAC method (~26.6 GPa) (Niu *et al.*, 2023). This convergence suggests that a kinetically hindered process may account for the much lower critical transition pressure (~12.6 GPa) in the first principle calculations without considering the detailed transition processes (Niu *et al.*, 2023).

Secondly, the ongoing debate between two models (reconstructive *vs.* martensitic) for the reidite formation requires atomic-scale analysis to elucidate the detailed relationship between the initial and product phases in a localized region. The martensitic-like mechanism (Kusaba *et al.*, 1985; Leroux *et al.*, 1999) may involve two instantaneous processes: a simple shear-induced transition into a quasi-scheelite structure and an additional minor readjustment process through diffusionless, cooperative atom movement, leading to the formation of lamellar (or twinned) reidite that has a clear crystallographic relationship with the zircon phase (Kusaba *et al.*, 1985; Kusaba *et al.*, 1986; Kelly and Rose, 2002; Timms *et al.*, 2017). In contrast, the diffusion-driven, reconstructive mechanism may involve substantial displacements and dramatic reordering, resulting in the loss of the relationship between the initial and product phases (Dmitriev *et al.*, 1988) as well as the epitaxial nucleation of granular or dendritic reidite from the host

(Erickson *et al.*, 2017; Cavosie *et al.*, 2018). The formation of dendritic reidite is more likely to occur in the later stages following the formation of lamellar reidite (Cavosie *et al.*, 2021), possibly due to a much slower, random walk-like diffusion compared to the more rapid martensitic transition. First principle calculations (Marqués *et al.*, 2008; Mihailova *et al.*, 2019; Stangarone *et al.*, 2019) support a reconstructive mechanism via an intermediate phase, especially at the thermodynamic transition pressure. However, phonon dispersion calculations suggest that the zircon phase can switch into the intermediate high-pressure low symmetry (HPLS) phase in hafnon without involving random atomic movement (Niu *et al.*, 2023). As compared to the techniques of electron backscatter diffraction (EBSD) (Erickson *et al.*, 2017) and conventional transmission electron microscopy (TEM) (Leroux *et al.*, 1999), high-resolution TEM (HRTEM) and corresponding fast Fourier transformation (FFT) techniques offer unique insights into the more detailed, atomic scale morphology and crystallographic relationship among different phases near the boundary, critical for unraveling the controversial reidite formation mechanism.

Thirdly, zircon grains with a wide range of damage-modified structures provide an exceptional way to investigate the interplay of radiation damage and high pressure on reidite formation. Depending on the amounts of U and Th and the elapsed time since incorporation, the internal irradiations from alpha-decay events of U and Th substitutional impurities in zircon (Pidgeon *et al.*, 1966; Meldrum *et al.*, 1998; Ewing, 2003; Valley *et al.*, 2014; Li *et al.*, 2021) cause structural changes that range from isolated defects in still crystalline material to being fully amorphous as the damage regions accumulate and overlap over geologic time (Chakoumakos *et al.*, 1987; Shuster *et al.*, 2006; Ewing, 2007; Farnan *et al.*, 2007; Farley *et al.*, 2011; Kusiak *et al.*, 2015). Generally, the applied pressure and temperature (Reid, 1969; Timms *et al.*, 2017; Cavosie *et al.*, 2018; Walton *et al.*, 2019) are the key parameters to originate reidite formation (Kusaba *et al.*, 1985; Leroux *et al.*, 1999). Due to the sensitivity of the material properties to the radiation-induced

structural change (Pidgeon *et al.*, 1966), the high-pressure response of materials can be modified by variations in the amount of radiation damage (Ewing, 2007; Lang *et al.*, 2009; Erickson *et al.*, 2017; Timms *et al.*, 2018). However, coupling radiation damage studies with high-pressure effects through the combined use of ion accelerators and high-pressure techniques is challenging (Glasmacher *et al.*, 2006; Lang *et al.*, 2008), although both high-pressure and irradiations by energetic ions can result in significant structural changes (Mao *et al.*, 2003; Glasmacher *et al.*, 2006; Zhang *et al.*, 2008; Lang *et al.*, 2009; Tracy *et al.*, 2015). Previous studies on natural specimens show the hindered formation of reidite in highly alpha-damaged zircon (Wittmann *et al.*, 2006; Reddy *et al.*, 2016; Erickson *et al.*, 2017; Timms *et al.*, 2018). However, there has been no systematic study of the formation of high-pressure phases that exhibit a wide range of radiation-damaged structures.

In this study, we investigate the coupled behavior of high pressure and pre-existing radiation damage by comparing a damage-free synthetic zircon reference sample with a variety of natural zircon grains that have experienced different degrees of alpha-recoil-damage and then subjecting a sample to approximately 16 pressure steps in a DAC spanning purported pressure range of zircon-reidite transformation. We use *in situ* synchrotron X-ray diffraction and complementary *in situ* Raman spectroscopy to provide quantitative information for a detailed description of the phase transition process from zircon to reidite as a function of pressure for crystals with a range of alpha-decay event doses. Monitoring the dynamic process of reidite growth is practically impossible using the shockwave method or natural reidite, because it requires a new sample whenever there is any change in applied pressure or radiation damage. We resolve this challenging problem using the *in situ* static DAC method, which allows an application of pressure over a continuous range in natural zircon samples with different degrees of radiation damage. The transition pressure converge from the three separate sources, *i.e.*, the static experiments of this work and previous studies

(van Westrenen *et al.*, 2004), natural reidite samples (Cavosie *et al.*, 2021; Wittmann *et al.*, 2021) and shockwave experiments (Fiske *et al.*, 1994; Erickson *et al.*, 2020a; Christoffersen *et al.*, 2023). The *in situ* static study shows that minor radiation damage dose enhances transformation to reidite, but severe damage one hinders it. We then examine the quenched DAC specimens additionally *ex-situ* by high-resolution transmission electron microscopy (HRTEM). This experiment provides direct information on the microstructural changes due to the interplay of high pressure and radiation damage from the alpha decay of incorporated actinides. We show that the occurrence and proportion of reidite are related to the pre-existing zircon alpha-decay event dose. Those findings have important implications for better understanding the mechanism of reidite formation and constraining the minimum pressure of hypervelocity impacts by reidite.

2. Materials and Methods

Five natural zircon specimens with different alpha-decay doses were used for the *in situ* XRD and Raman high-pressure experiments. The three specimens from Bancroft, Malawi, and Mud Tank were crushed into powers of 30-100 μm in grain size before the gamma-ray spectrometry, as measured in the paper of Eakin et al. (2016) where the activities and accumulated alpha radiation doses were obtained through ^{238}U via ^{226}Ra (^{214}Pb at ^{352} keV and ^{214}Pb at 609 keV) and ^{232}Th via ^{228}Ac (338 keV and 911 keV). Approximately 0.5 g of each size fraction, weighed to a precision of 0.1 mg, was placed in 10 ml graduated (1-10 ml) counting vials and counted in a high-purity germanium well. Refer to the cited paper for more details on the measurements and calculations. The alpha-decay dose was calculated as $6.9\pm0.7\times10^{16}$ α/g for a single crystal (1-2 cm wide) the fourth natural zircon from Pakistan using its concentrations of ^{238}U (28.2 ppm), ^{232}Th (19.3 ppm) and a corresponding age (615.4 Ma) as measured by Laser Ablation

Inductively Coupled Plasma Mass Spectrometry at the Institute of Tibetan Plateau Research, Chinese Academy of Sciences (CAS). External standards were NIST 610, NIST 612, and NIST 614. All samples and standards were corrected for change in the internal standard, ^{29}Si, throughout the run (Hasebe *et al.*, 2013). The measured concentrations are the mean from ablated pits with a diameter of ~50 μm. The minor variations in the measured concentrations of ^{238}U and ^{232}Th in different grains ensure the heterogeneity of ^{238}U and ^{232}Th in Pakistan zircon. The cathodoluminescence images did not show zoned structure in these four natural zircon samples, suggesting the approximately homogeneous distribution of U and Th in the zircon grains. We ensured the reliability of the alpha-decay event dose in this study by comparing it with a previous systematic Raman study of natural zircon by Zhang *et al.* (2000), sharing similar phonon frequencies and widths of the SiO_4 v_3 mode near 1008 cm^{-1} as a function of alpha-decay event dose (Table S1 and Supplementary Text 1). The alpha-decay dose of the fifth sample, a single crystal zircon (approximately 3 mm wide) synthesized by the flux method can be reasonably assumed to be 0 α/g.

In zircon, alpha-recoil nuclei (*e.g.*, 50-100 keV Pb) create a local accumulation of high defect concentrations by ballistic interaction between the incident-ion with surrounding atoms (*i.e.*, nuclear energy loss) (Weber *et al.*, 1997; Rios *et al.*, 2000; Ewing, 2007; Beirau *et al.*, 2016; Li *et al.*, 2017). However, for high-pressure behavior, it is technically difficult to simulate the radiation damage of alpha-recoils using external low-energy heavy ions (*e.g.*, 100 keV Pb), because they can reach only a depth of several tens of nanometers from the surface, which is unable to produce a homogeneously irradiated sample for most experimental measurements. In contrast, the alpha-recoil-induced damage throughout naturally occurring zircon provides a realistic condition for investigating radiation damage effects due to different U and Th concentrations and ages. The small lengthscales (<50 μm) of the zircon grains ensure statistical reliability for the assumption of approximately random distribution of U and Th in the sample

in DAC. Besides pressure and alpha decay event dose, temperature significantly influences the transformation to and reversion from reidite. However, the effect of radiation damage on reidite formation at elevated temperatures is relevant to natural impact environments but represents a significant technical challenge for laboratory studies. Realizing the three factors by DAC would be challenging, knowing the difficulties in coupling only two factors (alpha decay event dose and high pressure) through the combined use of ion accelerator and high-pressure techniques.

For the *in situ* micro-Raman measurements, a thin slice (~15 μm-thick and 50 μm-wide) was polished from a single-crystal zircon and loaded in a rhenium gasket sample chamber in a symmetrical DAC pressurized up to 41.7 GPa at room temperature. The experiments were conducted in a Renishaw InVia Reflex micro-Raman spectrometer at Peking University in China, with the 532 nm laser operated at 50 mW. Argon served as the quasi-hydrostatic pressure-transmitting medium and the pressure was monitored using ruby balls using an established method (Mao *et al.*, 1986). For each pressure step in the DAC, we increased 2-3 GPa in 1-2 min and completed collecting Raman signals in 3-5 mins.

The *in situ* high-pressure XRD measurements were carried out at room temperature at the 4W2 beamline of the Beijing Synchrotron Radiation Facility in China using a wavelength of 0.6199 Å at 20 keV, and a spot size of 30 μm. In order to avoid obvious diffraction spots from large grains in the XRD patterns, fine powders (~2 μm in size) crushed from the zircon grains were compressed into a thin slice (~15 μm thick). The quasi-hydrostatic conditions were provided by silicone oil. This medium allows convenience for sample loading but also significantly improves the chances of recovering the fine-powder thin slice for subsequent TEM experiments from the DAC pressurized up to 43.3 GPa. As the pressure is monitored by closely adjacent ruby balls, the types of transmitting medium generally do not affect the high-pressure measurements in materials (Bai *et al.*, 2019) including zircon (Knittle and Williams, 1993;

198 van Westrenen *et al.*, 2004; Nan *et al.*, 2022). We estimated the standard deviation of pressure (1σ) from
199 four adjacent ruby balls positioned at almost the same distance to the diamond center in a DAC, *e.g.*, ~0.3
200 GPa for applied pressures of 20-30 GPa, and ~0.4 GPa for applied ones of ~50 GPa when the distance of
201 the ruby ball is close enough to the sample (~10 μm). Two-dimensional patterns were collected using a
202 Pilatus3 2M detector within ~10 minutes after each of the required pressures was applied, and then
203 integrated with the software Fit 2d (Hammersley, 2016). The refinement of XRD data by the Rietveld
204 method was carried out with the Fullprof program (Rodríguez-Carvajal, 2001).

205 The TEM analysis was performed by a JEOL JEM-F200 at Institute of Tibetan Plateau Research,
206 CAS, on three representative zircon samples, *i.e.*, synthetic zircon (0 α/g), and natural zircon grains with
207 minor (6.9×10^{16} α/g) and severe damage (3.3×10^{19} α/g), before and after the high-pressure experiments.
208 Prior to being crushed into the fine grains (thickness < 0.2 μm for the convenience of TEM analysis)
209 between two glass slides and loaded onto the lacey-carbon thin film of a copper TEM grid, the thin slices
210 recovered from DACs subsequent to the high-pressure experiments were immersed in acetone for up to 3
211 h to fully remove possible contamination such as silicone oil. Alternatively, a 15 μm-thick and 100 μm-
212 wide synthetic-zircon grain recovered from 40 GPa-Raman experiments in DAC was cut into sectioned
213 slices with a uniform thickness of ~50 nm and a well-controlled zone axis by a microtome cutting method
214 (Li *et al.*, 2012).

215 HRTEM investigations require an ultra-thin sample (thickness <~50 nm) along an appropriate
216 crystallographic orientation (usually a major zone axis) to unambiguously determine the $ZrSiO_4$
217 polymorph and zone axis from atomic-scale resolution images and corresponding FFT patterns. Thus, the
218 experimentally determined FFT patterns (not shown in Fig. 1 for clarity, see Fig. S1) for each crystallite,
219 *e.g.*, from the area marked by the white dashed frame, were further compared to simulated FFT patterns

(see insets in Fig. 1).

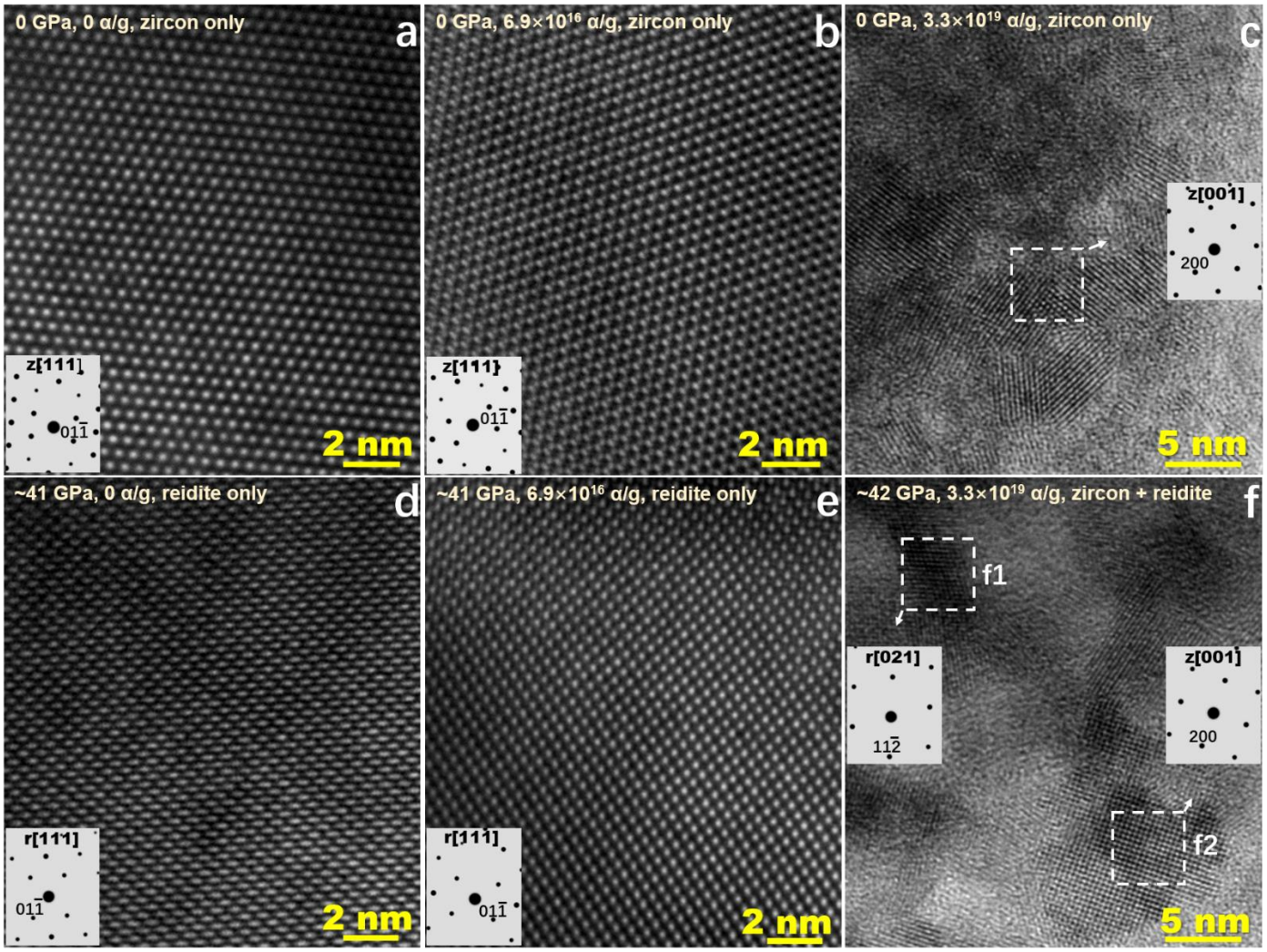

Fig. 1. HRTEM images of three representative zircon specimens before and after high-pressure experiments. The unpressurized zircon grains (**a**-**c**) compare with the corresponding recovered pressurized grains (**d**-**f**) from DACs at three different doses: 0 α/g (**a** and **d**), 6.9×10^{16} α/g (low alpha-dose, **b,** and **e**), and 3.3×10^{19} α/g (high alpha-dose, **c,** and **f**). The zone axis in the modeled (inset) and corresponding experimentally determined FFT (Fig. S1) marks the material structure. Both the unirradiated (**d**) and the low-dose (**e**) samples fully transform into reidite after zircon grains (**a** and **b**) are pressured to ~41 GPa. In contrast, the high-dose zircon sample, which consists of nanocrystals within an amorphous matrix (**c**) and is pressurized to ~42 GPa, shows a mixture of zircon and reidite nanocrystals within an amorphous matrix (**f**).

3. Results

3.1 High-resolution transmission electron microscopy

HRTEM and FFT techniques were used to characterize the microstructure and radiation damage in zircon grains in response to a range of alpha-recoil irradiations (with or without natural radiation damage) and subsequent high-pressure exposure and quenching to 1 bar. Before the high-pressure experiments, we conducted the atomic scale HRTEM analysis on three representative zircon specimens: (i) undamaged reference sample with 0 α/g (Fig. 1a), (ii) low-level damaged sample with 6.9×10^{16} α/g (Fig. 1b), and (iii) severely damaged sample with 3.3×10^{19} α/g (Fig. 1c) to show morphology of zircon grains modified by radiation damage. HRTEM images revealed an almost intact zircon structure in both the unirradiated (Fig. 1a) and the low-level damaged sample (Fig. 1b), which agrees with the previously reported threshold dose of 3×10^{18} α/g, below which only minor damage forms from the accumulation of isolated point defects (Murakami *et al.*, 1991; Zhang *et al.*, 2000). At higher alpha doses above this threshold, more severe damage in the form of zircon nanocrystals (5-20 nm) within an amorphous matrix was visible (Murakami *et al.*, 1991; Utsunomiya *et al.*, 2007) due to multiple overlaps of individual alpha-recoil damage cascades. However, even at 3.3×10^{19} α/g, as seen in Fig. 1c, zircon is not fully amorphous, likely due to thermal annealing at ambient conditions, similar to the previous HRTEM result (Utsunomiya *et al.*, 2007) of zircon grains at 1×10^{20} α/g.

After loading the samples irradiated to the same alpha decay-event doses (along with the unirradiated reference sample) in a DAC and pressing up to ~42 GPa, the resulting microstructures of quenched products (Figs. 1d-1f) were analyzed by HRTEM and compared with those obtained just by irradiation and no pressure exposure (Figs. 1a-1c). A complete pressure-induced phase transformation from zircon to reidite was evident in the unirradiated sample (Fig. 1d) and the low-dose sample (Fig. 1e) after quenching

257 from ~41 GPa. The intact lattice and periodic structure of the low-dose irradiated sample after
258 pressurization showed no recognizable differences from the unirradiated reference sample, despite alpha-
259 recoil irradiation before pressure exposure. In contrast, HRTEM characterization of the high alpha-decay
260 dose zircon sample after pressurization to a similar pressure ~42 GPa revealed a significantly different
261 morphology and microstructure (Fig. 1f). Similar to the unpressurized sample (Fig. 1c), there were no
262 large domains of intact structure remaining, but only separate nanocrystals (5-20 nm) as remnants from
263 severe damage overlap and formation of an amorphous matrix (Fig. 1f). Although some of the nanocrystals
264 were reidite (Fig. 1f and Fig. S1 *f*1), there were numerous nanocrystals that retained their zircon structure
265 (Fig. 1f and Fig. S1 *f*2), different from the complete transformation to reidite at almost the same pressure.
266 This difference shows a clear correlation between the amount of pre-existing radiation damage and the
267 reidite phase fraction that forms after subsequent pressurization.
268
269

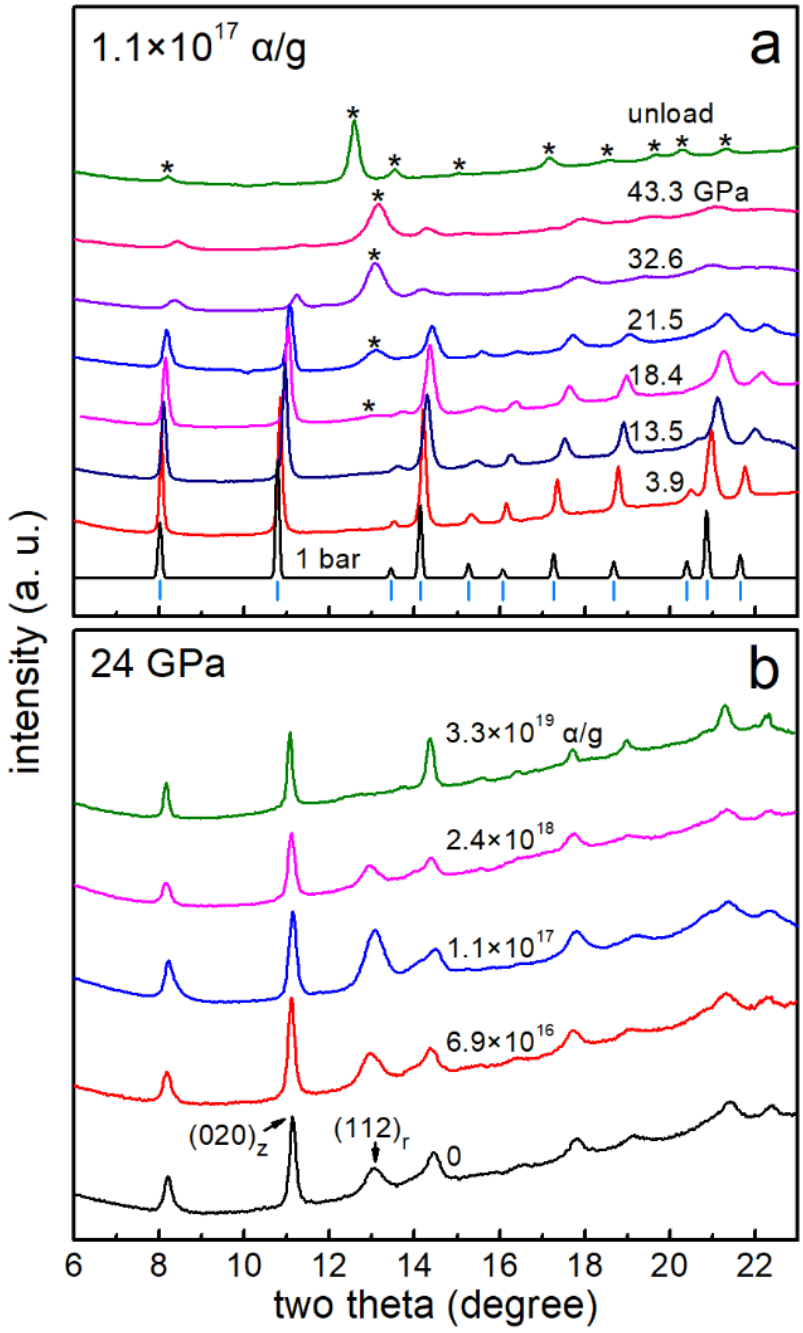

Fig. 2. Dependence of reidite formation on alpha-decay event dose as measured by *in situ* synchrotron XRD experiments in zircon grains pressurized in DACs. (**a**) A selected XRD pattern of a single-phase natural zircon (*e.g.*, 1.1×10^{17} α/g) shows the major Bragg peaks of the zircon structure at low pressure (marked by |). The transformation to reidite starts around 18.4 GPa (marked by *****) and completes after pressurization to 43.3 GPa, with the reidite phase being quenchable to 1 bar. (**b**) XRD pattern of irradiated zircon with increasing alpha-decay dose at 24 GPa. The relative intensity of reidite (112) and zircon (020), as marked by black arrows, can reflect the phase fraction of reidite.

3.2 *In situ* synchrotron XRD during DAC experiments

Pressurization of a moderately irradiated zircon (1.1×10^{17} α/g) shows a typical phase sequence under pressurization (Fig. 2a), as previously reported for undamaged zircon (van Westrenen *et al.*, 2004). This low-level radiation damage only produces isolated point defects in the zircon structure (Murakami *et al.*, 1991). At low pressures, the XRD pattern of the irradiated sample before pressure exposure shows no evidence of considerable radiation damage with the typical sharp diffraction maxima. The XRD patterns only show Bragg peaks representative of the zircon structure (marked by I), that is, (011), (020), (121), (112), (220), (022), (031), (013), (231), (132), and (040) following the sequence from low to high 2θ. At a pressure of 18.4 GPa, the first diffraction maxima typical for reidite are apparent, and they gradually increase with the further increase in pressure. At a pressure of 43.3 GPa, the zircon-to-reidite transformation has completed, as evidenced by the loss of all zircon Bragg peaks (Fig. 2a), and only diffraction maxima of the reidite structure (*****) are present in the XRD pattern, *i.e.*, (011), (112), (004), (020), (121), (015), (123), (024), and (220). In agreement with previous work, reidite is fully quenchable to ambient conditions (Lang *et al.*, 2008).

We compared the high-pressure phase fraction of several zircon grains with different alpha-decay doses, as quantified by the relative intensity of reidite (112) and zircon (020) planes, after pressing them to a similar pressure (for example, ~24 GPa in Fig. 2b). Under the equivalent compression conditions, moderately damaged samples show a distinct increase in the reidite phase fraction (maximum at 0.605 for 1.1×10^{17} α/g), but higher dose irradiations lead to an opposite effect of a rapid decrease in the reidite fraction (minimum at 0 for 3.3×10^{19} α/g). See detailed quantitative results at different pressures (21, 24, 32, and 36 GPa) showing the dependence of reidite formation on radiation damage in Supplementary Text 2 and Figs. S2-S4.

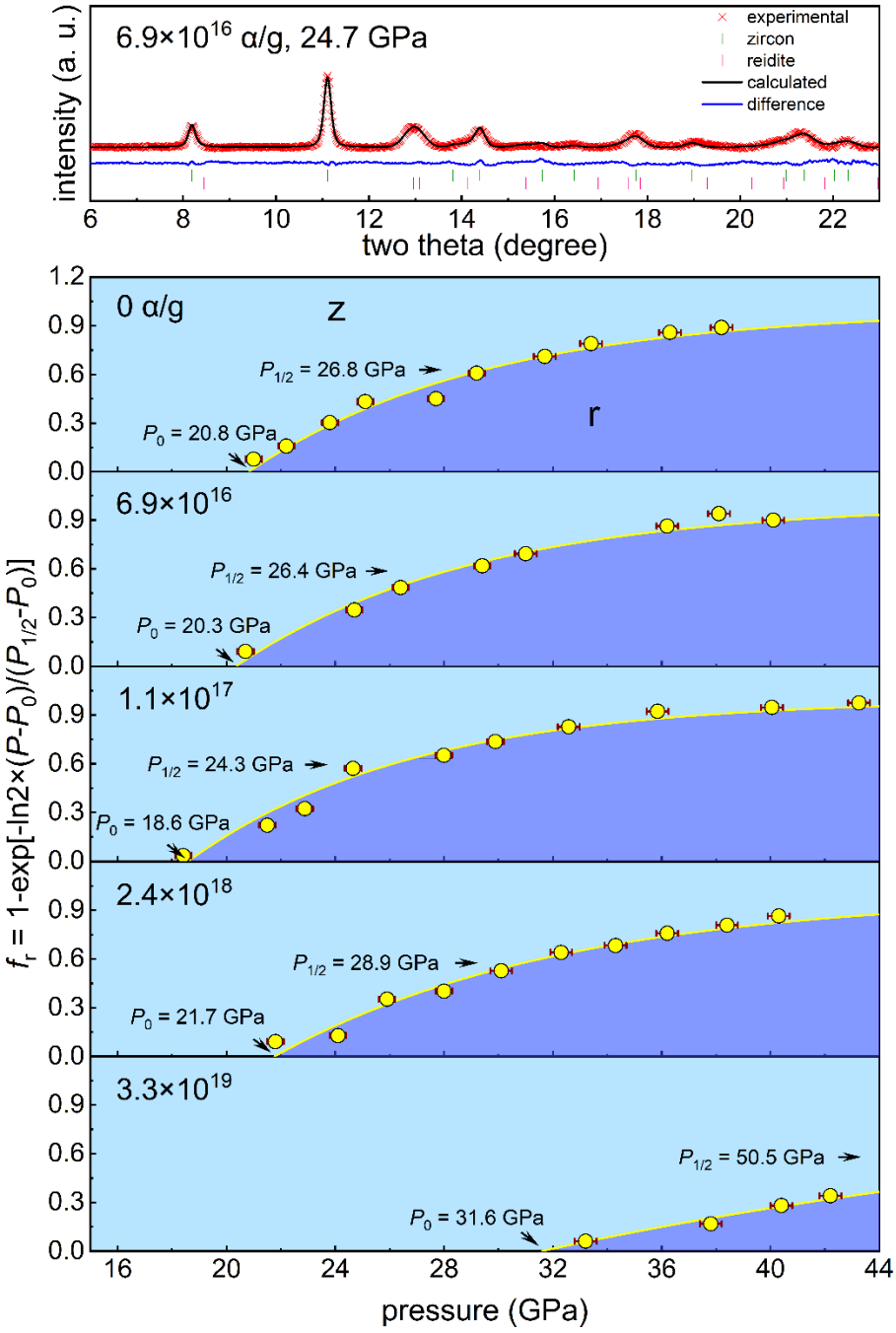

Fig. 3. The fraction of crystalline reidite, f_r, obtained from XRD data as a function of pressure and alpha-decay event dose. (**a**) A selected XRD pattern of a pre-damaged zircon sample (6.9×10^{16} α/g) measured at 24.7 GPa (red) and fitted by Rietveld refinement (black) using a mixed zircon and reidite phase shows good agreement as demonstrated by the difference curve (blue). (**b**) Reidite phase fraction (yellow circles) as obtained from the refinement of samples with different alpha-decay event doses and applied pressures. The increase in the reidite phase fraction with the pressure can be described by the equation $f_r = 1\text{-}\exp[-\ln2\times(P\text{-}P_0)/(P_{1/2}\text{-}P_0)]$ (yellow curves), with P_0 being the critical transition pressure for reidite and $P_{1/2}$ being the pressure at which half of the zircon transforms into reidite. With increasing alpha-decay dose, P_0 and $P_{1/2}$ decrease slowly to minimums at 1.1×10^{17} α/g, followed by a rapid increase for larger alpha-decay event doses.

315 **3.3 Reidite phase content quantification with Rietveld fitting of XRD data**

316 We obtained the relative crystalline phase fractions of reidite and zircon with a more quantitative
317 procedure by employing Rietveld refinement of XRD patterns measured at different pressures (Fig. 3a)
318 and over a range of accumulated alpha-decay event damage (Fig. 3b). There is no evidence of
319 decomposition into other crystalline phases (for example, ZrO_2 and SiO_2) induced by either pressure or
320 radiation, which is consistent with the previous results on alpha-damaged zircon grains (Murakami *et al.*,
321 1991; Leroux *et al.*, 1999; Wittmann *et al.*, 2006). Any contributions from radiation-induced
322 amorphization were removed with the XRD background in the patterns, as higher alpha-decay event doses
323 usually induce more amorphous phases due to the overlap of the recoil damage cascades. These two
324 conditions ensure that only considering the relative crystalline phase fractions of reidite and zircon, $f_r + f_z$
325 = 1, (with f_r marked by yellow circles in Fig. 3b) is largely valid in the quantification.

326 The relative reidite phase fractions are plotted against the corresponding pressure values, P, for all
327 the samples (Fig. 3). When compared at the same pressure (*e.g.*, 24 GPa) and when the alpha-decay event
328 dose is low, the fraction of reidite increases from 30.9% (0 α/g) and 34.3% (6.9×10^{16} α/g) to the maximum
329 of 48.1% (1.1×10^{17} α/g). Whereas, when the dose increases to 2.4×10^{18} and 3.3×10^{19} α/g, the fraction of
330 reidite decreases to 19.9% and ~0%, respectively.

331 Plotting of f_r as a function of P for all the samples can be best described by the following equation
332 (yellow curves in Fig. 3b):

333 $$f_r = 1 - \exp[-\ln 2 \times (P - P_0)/(P_{1/2} - P_0)] \quad (1),$$

334 using fitting parameters: P_0 (in GPa), the critical transition pressure for which reidite first appears, and
335 $P_{1/2}$ (in GPa), the pressure where half of the original zircon phase transforms into reidite. The darker blue
336 area below the yellow curve, as marked with "r" in Fig. 3b, represents the region of the crystalline phase

reidite. For all $ZrSiO_4$ samples, the fraction of reidite increases with increasing pressure above a critical transition pressure, as expected. For the reference zircon (0 α/g) and the zircon samples that were pre-damaged with increasing alpha-decay event doses of 6.9×10^{16}, 1.1×10^{17}, 2.4×10^{18}, and 3.3×10^{19} α/g, the corresponding P_0 were: 20.8, 20.3, 18.6, 21.7, and 31.6 GPa, respectively, and $P_{1/2}$: 26.8, 26.4, 24.3, 28.9, and 50.5 GPa, respectively (Fig. 4b and Table S1). Both P_0 and $P_{1/2}$ initially decrease to minimums at 1.1×10^{17} α/g (18.6 and 24.3 GPa, respectively) and then increase to maximums at 3.3×10^{19} α/g (31.6 and 50.5 GPa, respectively). Before the appearance of reidite at P_0 =31.6 GPa in the bottom panel (*i.e.*, at 3.3×10^{19} α/g) in Fig. 3b, the reidite fractions in the upper four panels are all >50%, indicating the significant hindrance of reidite formation by severe radiation damage. The closely adjacent ruby balls ensure that the pressure standard error (~0.3 GPa) is small enough for the trend of P_0 or $P_{1/2}$ to be resolved, particularly at 20-30 GPa before 2.4×10^{18} α/g.

In this zircon-reidite system, for any sample at any given pressure $P \geq P_0$, the pressure enhancement of $P_{1/2}$-P_0 can transform half of the remainder of the zircon into reidite. More specifically, the ratio of the zircon remainder after the transition 1-f_r has an exponential relationship with the actual pressure enhancement P-P_0 divided by the enhancement $P_{1/2}$-P_0,

$$1 - f_r = (1/2)^{(P-P_0)/(P_{1/2}-P_0)}. \quad (2).$$

Simple transformation shows that Equation (2) equals the fitted Equation (1), suggesting the random occurrence of reidite in the zircon matrix according to P, P_0, and $P_{1/2}$. In contrast with the above-mentioned visual estimation (Fig. 2), Rietveld refinements of all XRD data combined with Equation (1) is a more appropriate approach to describe the effect of radiation damage on the formation using P_0 and $P_{1/2}$.

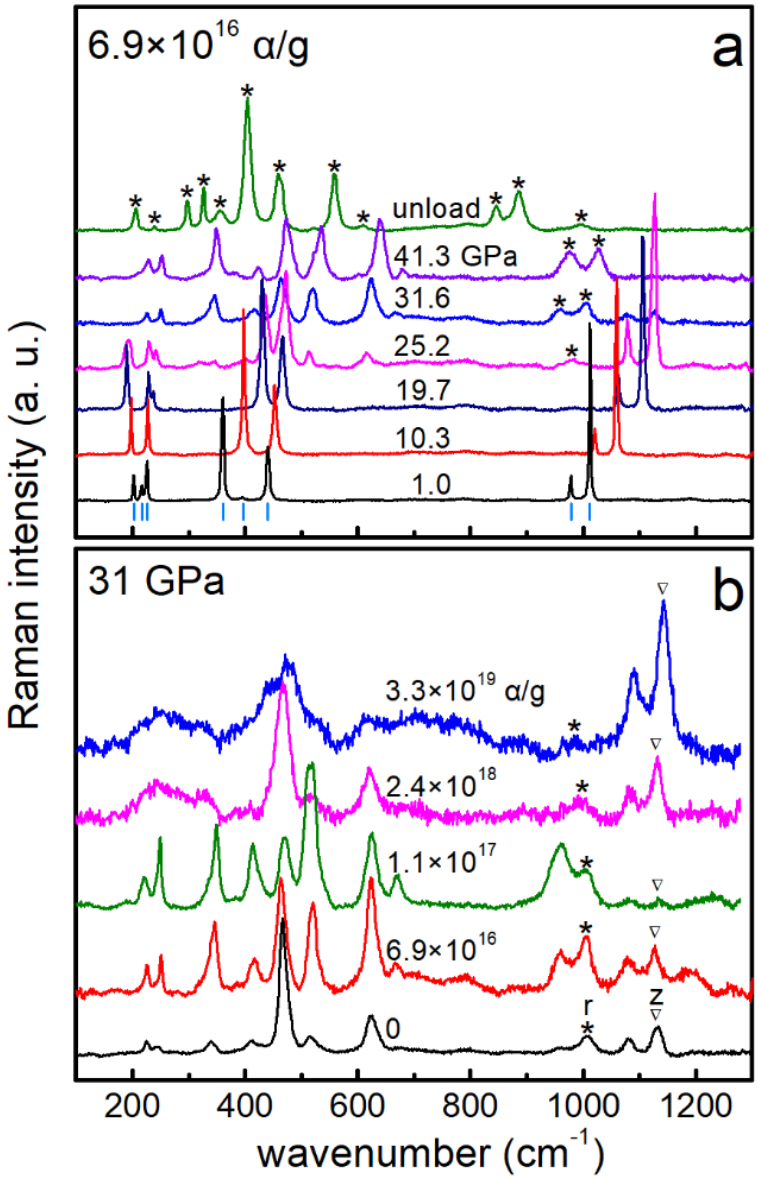

Fig. 4. ***In situ*** **Raman spectra of zircon pressurized in DACs revealing the influence of radiation damage on the formation of reidite.** (**a**) Selected spectra of a single-phase natural zircon (6.9×10^{16} α/g, and its main modes marked by | at 1.0 GPa) show an increasing amount of reidite with increasing pressure ($P \geq 25.2$ GPa), as evidenced by the gradual growth of modes that are characteristic of the reidite high-pressure phase (major modes marked by*: 559, 844, and 884 cm^{-1} at 1 GPa). (**b**) Raman spectra of zircon irradiated with increasing alpha-decay events from 0 – 3.3×10^{19} α/g compressed to the same pressure of ~31 GPa. The relative intensity of the reidite mode near 1000 cm^{-1} (*) and the zircon mode near 1135 cm^{-1} (▽) increases with increasing radiation damage up to 1.1×10^{17} α/g and decreases for larger alpha-decay event doses.

3.4 *In situ* Raman spectroscopy during DAC experiments

We characterized the synthetic zircon with the four natural zircon specimens with alpha-decay damage pressurized in DACs in situ by Raman spectroscopy at approximately 16 different pressure steps. Fig. 4 shows the dependence of reidite formation as a function of pressure and alpha-decay event dose, similar to the XRD measurements. The observed Raman peaks at low pressure (*e.g.*, 1.0 GPa) all coincide with the main vibrational modes of zircon (marked by vertical blue lines, |) (Zhang *et al.*, 2000): 202, 215, 226, 361, 394, 439, 977, and 1012 cm^{-1} (Fig. 4a), with no other phases or impurities detected in the zircon samples before pressurization. Before pressurization, the SiO_4 v_3 stretching mode at 1008 cm^{-1} shifts to lower wavenumbers, accompanied by the gradual broadening of the full width at half maximum (FWHM) for higher level radiation damage. The rates of shift and broadening as a function of alpha-decay event dose are in good agreement with a previous Raman study (Zhang *et al.*, 2000) (see Table S2 for the comparison). Upon increasing pressure, as shown in Fig. 4a for the sample with 6.9×10^{16} α/g, the zircon phase fully transforms at 41.3 GPa into single-phase reidite, which is quenchable after pressure release cf. Knittle and Williams (1993). The reidite vibrational modes indicated in the quenched spectrum are at 206, 240, 298, 327, 357, 404, 459, 559, 609, 844, 884, and 1001 cm^{-1} (marked by*); the absence of any mode of other phases demonstrates that the zircon fully transformed into reidite (Knittle and Williams, 1993). The thermodynamic calculations of Timms *et al.* (2017) show that the zircon dissociation reaction has a steep Clapeyron slope and is effectively a high-temperature, low-pressure phenomenon. Consistent with previous studies at room temperature (Kusaba *et al.*, 1985; Leroux *et al.*, 1999; Wittmann *et al.*, 2006), there is no evidence of dissociation of zircon to ZrO_2 and SiO_2 pressurized up to ~40 GPa. These peak positions systematically shift to higher wavenumbers with increasing pressure.

The critical transition pressure for reidite formation, determined by the first appearance of

characteristic Raman modes, is 26.8 GPa for the unirradiated reference sample and initially decreases to 25.2 GPa for 6.9×10^{16} α/g and 20.3 GPa for 1.1×10^{17} α/g followed by an increase for the more severely damaged zircon samples to 23.2 GPa for 2.4×10^{18} α/g and 28.6 GPa for 3.3×10^{19} α/g (as detailed in Table S1). This trend is consistent with the synchrotron XRD measurements, but the critical transition pressures are somewhat higher for the Raman data reported previously (Mihailova *et al.*, 2019). We can rule out the possible influence by medium or an artefact of the Raman facility, as all the synthetic zircon samples (0 α/g) with different pressure transmitting media and Raman facilities start to transform to reidite at the same applied pressure around 26 GPa, as detailed in a recent paper by Nan *et al.* (2022). Raman is sensitive to bond stretching, whereas XRD is sensitive to structural change near a critical pressure. This difference may account for the "approximately" consistent higher values (~ 5 GPa) (Table S1) via Raman spectroscopy.

We quantitatively assessed the influence of radiation damage on reidite formation at a given pressure of 31 GPa (Fig. 4b) by the relative peak intensities of the SiO_4 asymmetric stretching mode v_3 in both phases. Note that the peak at ~884 cm^{-1} in unpressurized reidite shifts to ~1000 cm^{-1} at 31 GPa, and the peak at ~1008 cm^{-1} in unpressurized zircon shifts to ~1135 cm^{-1} at 31 GPa. Gucsik *et al.* (2004) used this approach in previous Raman studies on the zircon-reidite phase transition in unirradiated zircon samples. The relative peak intensity at 31 GPa gradually increases from 0.62 for the unirradiated zircon sample to 1.82 for the 6.9×10^{16} α/g sample until a maximum reaches at 4.29 for the 1.1×10^{17} α/g sample. The peak intensity decreases again for a higher level of radiation damage to 0.38 and 0.13 for the 2.4×10^{18} α/g and 3.3×10^{19} α/g samples, respectively. These findings by XRD, HRTEM, and Raman are consistent with previous studies of shock metamorphosed zircon grains, showing that the loss of crystallinity at severely damaged zircon is likely suppressing the formation of reidite (Wittmann *et al.*, 2006; Reddy *et al.*, 2016;

Erickson *et al.*, 2017; Timms *et al.*, 2018). However, the present work also reveals an opposite process, *i.e.*, the enhanced reidite formation by minor radiation damage.

4. Discussion

4.1 Formation mechanism of reidite

The zircon-reidite phase transition has been considered a martensitic-type transition (Kusaba *et al.*, 1985; Leroux *et al.*, 1999). However, there is opposite evidence of the reconstructive, diffusion-controlled transformation mechanism (Dmitriev *et al.*, 1988), rather than a simple martensitic one that typically has only one habit plane (or interface) between the initial and product phases in minerals due to their low symmetry (Kirby and Stern, 1993), as detailed in Supplementary Text 3.

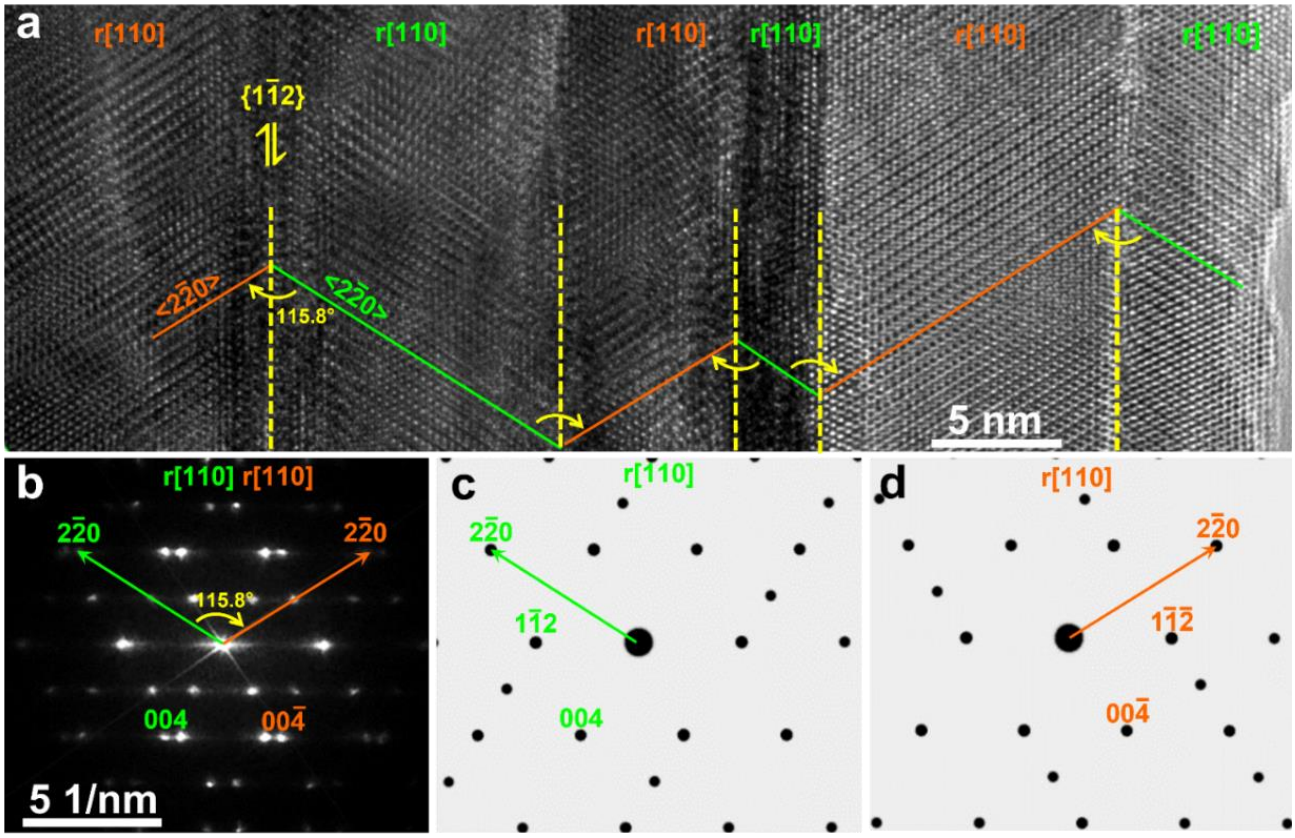

Fig. 5. The atomic structure of twinned reidite in synthetic zircon recovered from 40 GPa in DAC. The HRTEM image (**a**) shows that two types of reidite plates, with the same zone axis along [110], alternatingly occur with a changing interval (marked by orange and green lines along <2$\bar{2}$0>) and a fixed angle (115.8°) between two adjacent plates. The FFT pattern (**b**), as obtained from **a**, matches well with the sum of two simulated FFT patterns (**c**, in green) and (**d**, in orange). The double arrows (in **a**) represent opposite shear components of shear strain along the boundary of a twin, unambiguously evidencing that reidite formation in DAC is also a martensitic-type transition, and there is internal stress-induced phase transition (Kelly and Rose, 2002).

Based on the rate (~1.5 GPa/min) of applied pressure increase during the DAC experiments, the formation of reidite in DAC occurs at much longer durations that may favor the diffusive-type phase transition, different from the microsecond scale transition in shocked samples where the rapid martensitic phase transition is more likely to occur. However, in this work, we observe atomic-scale twinned structures of reidite by HRTEM and FFT in a synthetic zircon recovered from a 40 GPa static experiment (Fig. 5), consistent with the characteristic internal stress-induced martensitic transition illustrated in Fig. 6 of the

445 paper by Kelly and Rose (2002). The stress buildup favors the nucleation of self-accommodating variants
446 with opposing shear strains. Opposite internal stresses (as marked by double arrows along <1$\bar{1}$2> in Fig.
447 5a) are produced along the boundary of twins when the shear strain is generated by the initial reidite plate
448 induced by external stress. After the instantaneous formation of the initial reidite plate, the internal stress
449 switches to the opposite direction, thus guiding the cooperative atomic movement rather than the random
450 walk-like diffusion and forming the next reidite plate with a clear crystallographic relationship with the
451 initial plate. Thus, the characteristic twinned structures and corresponding FFT images provide critical
452 information on understanding the detailed phase transition processes at the atomic scale, unambiguously
453 evidencing an internal stress-induced martensitic-type reidite formation mechanism in DAC. In shock
454 metamorphosed zircon grains, a twin structure of reidite has also been found by conventional TEM images
455 and corresponding electron diffraction patterns (Leroux *et al.*, 1999). Cavosie *et al.* (2015) used electron
456 backscatter diffraction to show the micrometer-sized shock-twinned zircon and reidite in natural reidite,
457 where this twin structure has not yet been found by TEM, likely due to the smaller volume fraction of
458 reidite grains. All these results suggest that the three different sources, from natural samples, static, and
459 shockwave experiments, share a similar mechanism of reidite formation.

460 According to Kelly and Rose (2002) and Cohen *et al.* (1979), the random walk of atoms in a
461 reconstructive, diffusion-controlled transformation significantly contrasts with the rapid, shear-induced
462 diffusionless structural change for a martensitic transformation. Thus, diffusive type transition is unlikely
463 to occur and even fully complete on the scale of microseconds, as observed in the shockwave experiments
464 in zircon (Leroux *et al.*, 1999). However, diffusive type transitions, such as the epitaxial nucleation of
465 dendritic reidite on the lamellae (Cavosie *et al.*, 2018), may occur at a later stage with a long formation
466 duration. This topic is worth future careful investigations, particularly by the technique of HRTEM on the

crystallographic relationship among different phases of natural reidite.

4.2 Reidite formation modified by alpha-damage

Similar to the formation of twin structures induced by internal stress (Kelly and Rose, 2002), the nucleation of the martensitic transition likely occurs in regions of higher stress concentration near the core, induced by alpha-recoil damage. This is likely due to the reduced energy barrier for nucleation caused by the stored strain energy of the damaged zircon. The nuclear collisions between alpha-recoils and the surrounding atoms produce "cascades" of displacements or atomic movements (Geisler *et al.*, 2001; Ewing *et al.*, 2003; Geisler *et al.*, 2003), accompanied by rotation of the SiO_4 tetrahedra in zircon (Farges and Calas, 1991; Leroux *et al.*, 1999), resulting in strain fields around the damaged domain. Strain fields due to ion irradiation are well-documented for many materials (Murakami *et al.*, 1991; Vetter *et al.*, 1998; Miro *et al.*, 2005; Zhang *et al.*, 2019; Zhang *et al.*, 2020). For example, in GeS, the non-uniform strain distribution generates local stress perturbations around the damaged track core, as shown by an HRTEM image of four strain contrast centers situated 10-20 nm from the track core (Vetter *et al.*, 1998).

Besides the radiation damage-induced strain fields, there are several structural considerations, *e.g.*, minor atomic displacements (Kusaba *et al.*, 1986) and the intactness of the zircon structure (Wittmann *et al.*, 2006) that are critical to the growth of the reidite phase. Kusaba et al. (1986) proposed that the displacive-type martensitic transition requires only minor atomic displacements facilitating the rotation of SiO_4 tetrahedra and the atomic readjustment into the ideal scheelite structural arrangement. An intact structure of zircon ensures that a coherent shear strain is retained during pressure-induced distortions (Wittmann *et al.*, 2006) and that the requirement of continuity between the two phases is satisfied for the growth of the product phase (Kelly and Rose, 2002). Based on this scenario, as well as the alpha-decay

event damage accumulation in zircon as proposed by Murakami et al. (1991), we can explain the observed distinct behaviors of the zircon-reidite transition over a range of alpha-decay event doses.

For the unirradiated zircon (0 α/g), almost no alpha-recoil-induced displaced atoms and associated elastic strain fields from defects exist, and the zircon structure is fully intact. The intactness of the zircon structure is critical to assuring the connectivity of habit planes required to attain the elastic energy (Wittmann *et al.*, 2006; Erickson *et al.*, 2017; Timms *et al.*, 2018) for rapid martensitic transformation. However, the absence of alpha-decay events does not allow the production of additional point defects or strain fields by radiation damage to enhance the phase transition.

In contrast, only isolated defect regions exist within the matrix for the zircon grains with low levels of accumulated alpha-decay damage. For example, at an accumulated alpha-decay dose of $D = 1.1\times10^{17}$ α/g, only 0.03 displacements per atom (or dpa) are displaced from their original sites under the assumption of 5,000 displacements per alpha-decay event (Farnan *et al.*, 2007). At such low damage levels, some SiO_4 tetrahedra distort as the isolated local strain fields build up. However, the overall coherency of the zircon structure remains intact, as evidenced by the HRTEM results (Fig. 1b) and previous studies (Farges and Calas, 1991; Murakami *et al.*, 1991). These results also agree well with other types of measurements: Nano-indentation measurements (Beirau *et al.*, 2016) showed that zircon grains with a low-level alpha-decay event dose (7.5×10^{16} α/g) have an increased hardness with an elastic stiffness that is similar to that of undamaged zircon. The Raman results (Zhang *et al.*, 2000) show a general increase in the wavenumber of the Si-O stretching mode near 1008 cm^{-1} with increasing alpha-recoil damage up to 7.5×10^{18} α/g but an almost unchanged wavenumber at alpha-decay event doses between 0 and 1×10^{18} α/g. Thus, at minor damaged zircon (*e.g.*, 6.9×10^{16} and 1.1×10^{17} α/g in this work), the local stress surrounding individual damage cascades can assist in the growth of reidite under pressure. The elastic stiffness is almost

511 unchanged for the low-level irradiation, allowing higher pressure attained in the lattice for reidite
512 formation (Timms *et al.*, 2018). Provided the zircon structure remains intact, the minor displacements due
513 to radiation damage facilitate atomic adjustments to complete the reidite formation according to the ideal
514 scheelite structure. More specifically, the local internal stresses, generated by isolated radiation-damaged
515 domain, initiate the nucleation of the reidite phase and its subsequent growth. Individual damage cascades
516 lower the activation barrier for reidite formation, resulting in a lower critical transition pressure than the
517 undamaged zircon.

518 The situation is dramatically different for severely damaged samples with the accumulation of a high
519 alpha-decay event dose (*e.g.*, 3.3×10^{19} α/g). As experimentally observed by HRTEM in Fig. 1c, only
520 isolated zircon nanocrystals remain within an amorphous matrix due to the significant overlap of alpha-
521 recoil cascades. The severely damaged zircon samples have a reduced coordination of Zr, contain isolated
522 SiO_4 tetrahedra, and experience a complete loss of the SiO_4 and ZrO_8 edge-sharing framework (Farges
523 and Calas, 1991; Woodhead *et al.*, 1991; Farnan and Salje, 2001). The radiation damage decreases the
524 modulus and anisotropy of the highly damaged zircon with a high-level alpha-decay event dose up to
525 7×10^{18} α/g (Özkan, 2008; Timms *et al.*, 2018). The high alpha doses lead to inability to support high
526 pressure for a given elastic strain due to a reduction in elastic stiffness. The disorder, or the total loss of
527 the long-range zircon structure causing loss of elastic stiffness and anisotropy (Timms *et al.*, 2018), or the
528 connectivity of habit planes to attain the elastic energy (Wittmann *et al.*, 2006), inhibits the transition to
529 reidite. As obtained by the DAC method, the higher critical transition pressure and lower reidite fraction
530 in heavily damaged samples (Fig. 3) than those of undamaged zircon (Figs. 2b and 4b) coincide with
531 previous observations in naturally-occurring reidite (Wittmann *et al.*, 2006; Timms *et al.*, 2018).

532 Since a low dose of alpha decay facilitates the formation of reidite and a high alpha dose hinders it,

there must be a critical alpha-decay event dose where the behavior changes. Based on XRD results (Fig. 3), the critical alpha-dose lies between 1.1×10^{17} and 2.4×10^{18} α/g. At this alpha dose, there is a balance between promoting the phase transition by displaced atoms from alpha-recoil damaged domains and preventing the phase transition due to losing the continuity of the habit plane. The turning point (~1×10^{18} α/g) observed in the high-pressure experiments of this work is consistent with the percolation threshold of ~1.7×10^{18} α/g measured by electron microprobe (Geisler *et al.*, 2003) and ~2×10^{18} α/g by helium diffusivity measurements in zircon (Guenthner *et al.*, 2013). Helium diffusivity initially decreases with increasing alpha decay event dose, followed by a rapid diffusivity increase after passing the turning point (Guenthner *et al.*, 2013), validating independently the reverse effects of radiation damage on reidite formation observed in this work. The most common impurities in zircon are Hf, U, and Th. Although the Hf impurity in zircon may cause additional structural changes, the low level (<3 mol%) is not sufficient to cause observable phonon frequency shifts (Zhang *et al.*, 2000) and significant differences in high-pressure behavior (Niu *et al.*, 2023) due to the similarities between hafnon ($HfSiO_4$, $I4_1/amd$) and zircon. As the concentrations of U and Th are much lower (<1000 ppm), the direct influence on the structure of zircon is minimal. However, the damage from the alpha decay of U and Th significantly influences the high-pressure transition to reidite.

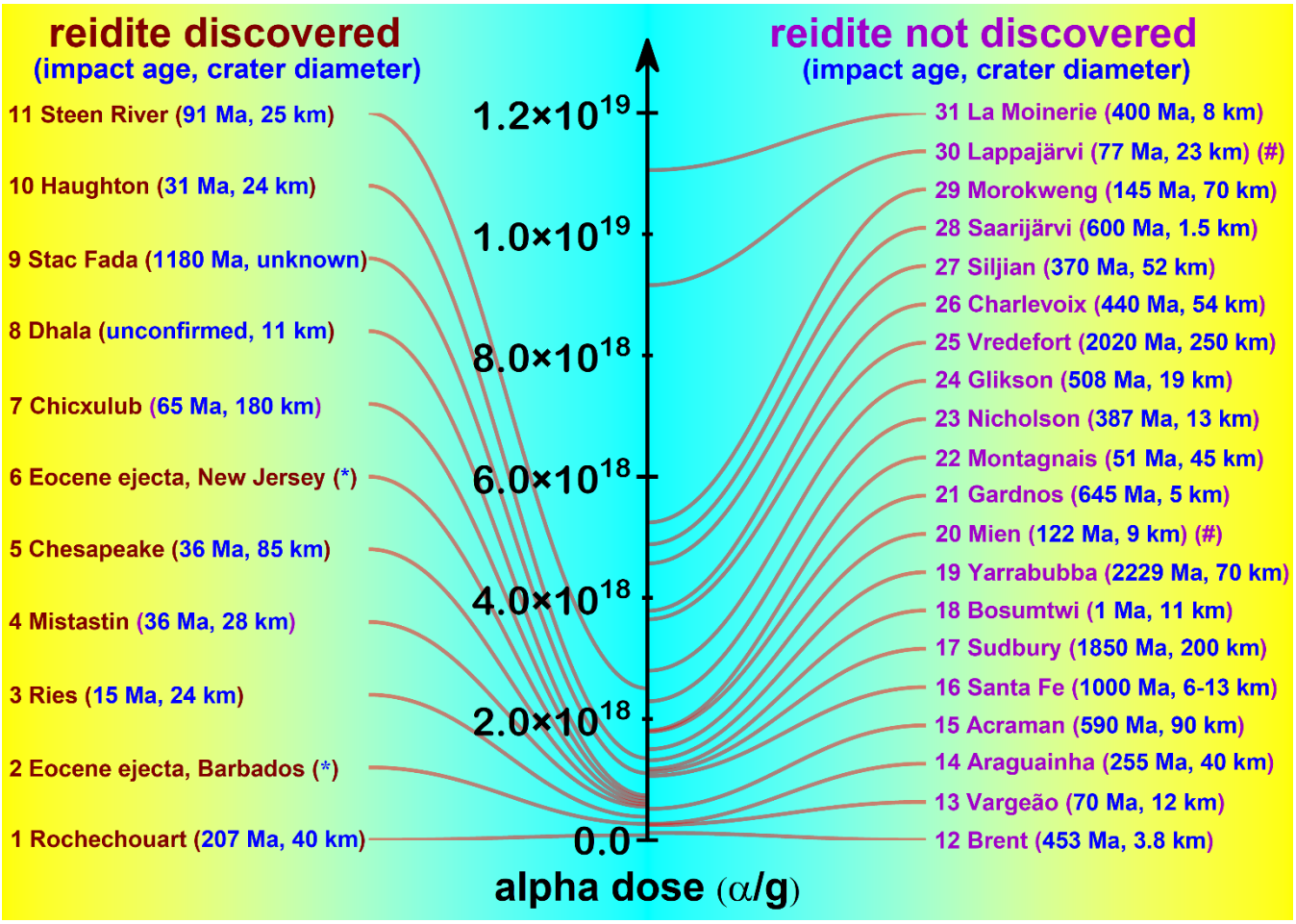

Fig. 6. The correlation between the occurrence of reidite and the pre-impact alpha-decay event dose in zircon at the reported impact structures. The zircon U-Pb analysis shows the preferential formation of reidite at the eleven impact structures (marked by 1-11 in the left column) with minor alpha-decay damage in zircon before the impact event. The unlisted four reidite sites (Xiuyan, Rock Elm, Woodleigh, and Gosses Bluff) are due to no published U-Pb data available for zircon (Chen *et al.*, 2013; Cavosie *et al.*, 2015; Cox *et al.*, 2018; Cousins *et al.*, 2022). The other twenty sites, marked by 12-31 in the right column, represent the ~190 reported craters without identified reidite, showing a wide range of alpha-decay doses. Sites 2 and 6 (as marked by*) originated from Site 5 (Glass and Liu, 2001; Glass *et al.*, 2002). Sites 20 and 30 (marked by # as a subcategory) are craters with FRIGN zircon identified but without reidite identified.

4.3. Implications

We compared the alpha-decay event doses that had accumulated before the impact events among natural zircon samples in target rocks of terrestrial impact structures, both with and without identified reidite (Fig. 6), showing the preferential occurrence of natural reidite in the reported impact structures

where the precursor zircon has more relatively low alpha-decay event dose. The average pre-impact alpha dose was estimated by the difference in the alpha-decay event dose between the U-Pb age and the impact age using the method of Holland and Gottfried (1955) and published zircon U-Pb data (including U, Th, and Pb concentrations) from the impactites and impact structures (Tables S3 and S4, and Supplementary Excel files 1 and 2). Among all the fifteen sites with identified reidite, eleven sites (as marked by 1-11 and listed in the left column) have a relatively lower alpha-decay dose (2.7×10^{17} – 2.5×10^{18} α/g); the four unlisted reidite sites (Xiuyan, Rock Elm, Woodleigh, and Gosses Bluff) (Chen *et al.*, 2013; Cavosie *et al.*, 2015; Cox *et al.*, 2018; Cousins *et al.*, 2022) do not have published U-Pb data for zircon. This result from natural reidite implies the enhanced formation of reidite for zircon with light radiation damage, consistent with our findings by the DAC method. In contrast, a wide range of alpha-decay doses (1.2×10^{17} – 1.1×10^{19} α/g) for the twenty sites in the right column (marked by 12-31) represents ~190 reported craters at which reidite has remained unidentified.

Granular zircon in impactites can preserve crystallographic evidence of the former presence of reidite (Timms *et al.*, 2017), which has been termed 'former reidite in granular neoblastic (FRIGN) zircon (Cavosie *et al.*, 2018). FRIGN zircon forms by initial transformation to reidite along unique orientations and subsequent reversion to neoblastic zircon by high temperature during the impact, as evidenced by the appearance of ZrO_2 (Timms *et al.*, 2017; Cavosie *et al.*, 2018). FRIGN zircon appears at a growing number of sites, including Chicxulub (Zhao *et al.*, 2021), Rochechouart (Plan *et al.*, 2021), and Gosses Bluff (Cousins *et al.*, 2022) where both reidite and FRIGN zircon co-exist in the same zircon. Among the above three co-existed sites, Gosses Bluff is the only site unlisted in the left column due to the absence of U-Pb data. FRIGN zircon also appears at impact sites where no reidite has been identified, including Meteor Crater (Cavosie *et al.*, 2016), Acraman (Timms *et al.*, 2017), Yarrabubba (Erickson *et al.*, 2020b),

589 Lappajärvi (Kenny *et al.*, 2019), Mien (Martell *et al.*, 2021), Australasian tektites (Cavosie and Koeberl,
590 2019), and others. However, neoblastic granular zircon may not preserve the U and Th of the original
591 grain, impeding reliable alpha dose calculations to be made, even if the target rock age is known.

592 The above analysis is only the first practical step in connecting our static experimental findings with
593 the natural occurrence of reidite by estimating the average pre-impact dose based on the currently
594 available published data. However, the actual situation in naturally-occurring reidite is more complicated.
595 A more accurate estimate requires detailed knowledge of the impact age, variations in U-Pb data within
596 and among different grains, the geological history at a given crater, the different shock physics responses
597 of porous *vs.* crystalline target rocks (Kowitz *et al.*, 2016), and the effects of shock impedance amongst
598 co-existing phases (Wittmann *et al.*, 2021). Unfortunately, many datasets related to radiation damage are
599 still unavailable for zircon at the known impact sites, especially for the ~190 known impact structures in
600 which reidite remains undiscovered. Moreover, reidite has been found in shocked rocks, ejecta deposits,
601 and a lunar meteorite (Xing *et al.*, 2020); the applicability of Equation (1) to different environments thus
602 needs careful testing. However, the bottom line is that one should consider the effect of alpha-recoil
603 damage to constrain the minimum pressure for these reidite occurrences. We infer that with additional
604 related data input in the future, more reidite is promising to discover in samples from these craters
605 currently listed in the right column with a low level of accumulated alpha-decay damage. We can then
606 move these craters to the left column. For example, reidite was recently reported at the Mistastin impact
607 structure by Tolometti *et al.* (2022).

608 Nevertheless, equation (1) allows one to predict f_r for a given pressure P_0 based on the amount of pre-
609 existing radiation damage from alpha decays (in α/g) in a zircon sample. For example, a zircon pre-
610 damaged with 1.1×10^{17} α/g, P_0 =18.2 GPa, and $P_{1/2}$ = 22.8 GPa yields ~90% of reidite at P = 36 GPa,

while a zircon pre-damaged with 3.3×10^{19} α/g, P_0 = 31.6 GPa and $P_{1/2}$ = 50.5 GPa yields merely ~20% at the same pressure of 36 GPa. Recently, Cavosie et al. (2021) estimated a formation pressure of 40 GPa for a zircon that was near-fully transformed to reidite from the Chesapeake ejecta horizon based on available data from shock recovery experiments (Kusaba *et al.*, 1986; Fiske *et al.*, 1994; Wittmann *et al.*, 2006). The estimated pressure (40 GPa) from the measured percentage of 89% of natural reidite (Cavosie *et al.*, 2021) has an uncannily similar result to our estimate of ~90% reidite at 36 GPa by using Equation (1) when assuming a pre-impact dose of 1.1×10^{17} α/g. The data also converge at the critical transition pressure ~20 GPa at which the transition starts (or the reidite percentage is ~1 %) for the three different sources, *i.e.*, static experiments in this work (Fig. 3) and a previous study (van Westrenen *et al.*, 2004), shockwave experiments (Fiske *et al.*, 1994), and natural reidite samples (Cavosie *et al.*, 2021; Wittmann *et al.*, 2021). It is a rare convergence when the data from three separate sources agree remarkably well, which validates the new DAC data on the radiation effects on reidite formation.

Despite the much longer pressurization durations of the static experiments that favor a diffusive mechanism, the static results from *in situ* DAC (Figs. 2 and 4) and *ex-situ* HRTEM experiments (Fig. 5) complement the shockwave metamorphosed results *via* a unique way to describe atomic scale reidite growth process. Although the static, the shockwave, and the naturally-occurring specimens have different pressurization timescales and environments, the three sources show a similar twin structure. The atomic scale alternating opposing shear strains along the boundary of the twinned reidite in the static sample (Fig. 5) provide information necessary for a deeper understanding of the reidite formation mechanism (*e.g.*, the nucleation and subsequent growth of twinned reidite) in shockwave metamorphosed zircon. Despite the importance of understanding the formation mechanism and the promise of constraining the minimum pressure during hypervelocity impacts, we cannot use the static method to simulate reidite transformation

633 during the hypervelocity impact events since they have different pressurization and depressurization
634 (shock-release) timescales and environments.

635 In summary, we have demonstrated that the amount of accumulated self-radiation-damage controls
636 the zircon-to-reidite phase transition pressure. Natural zircon grains show wide variability in U and Th
637 composition; hence, there is a range in alpha-decay event dose from 6×10^{16} to 1.5×10^{20} α/g (Murakami *et*
638 *al.*, 1991; Utsunomiya *et al.*, 2007), depending on the age and composition of zircon. One should consider
639 the amount of radiation damage when using the occurrence of reidite and its phase fraction to constrain
640 the minimum pressure that occurs during hypervelocity impacts. At low doses, radiation-induced atomic
641 displacements and strains facilitate the re-adjustment of atoms and the rotation of SiO_4 tetrahedra into the
642 scheelite-structured $ZrSiO_4$ - reidite, thus enhancing the phase transition. At high doses, however, the
643 phase transition to reidite is hindered in the absence of large domains of intact zircon structure that can
644 accommodate the coherent stresses required to complete the martensitic transformation into the scheelite
645 structure. The atomic structures of twinned reidite show the alternating occurrence of two types of reidite
646 plates, evidencing a local internal stress-assisted martensitic phase transition. The enhanced reidite
647 formation by minor radiation damage observed in the static experiments is consistent with the higher
648 occurrence of reidite at impact sites for which zircon has a relatively lower alpha-decay-dose before the
649 impact event. We describe the reidite fraction as a function of pressure for zircon and alpha-decay events
650 by an exponential equation, having promise for constraining the minimum pressure during hypervelocity
651 impacts (Fig. 6).

652

653 **Declaration of interests**

654 The authors declare that they have no known competing financial interests or personal relationships

655 that could have appeared to influence the work reported in this paper.

656

657 **Acknowledgements**

658 This work is supported by National Key Research and Development Program of China
659 (2022YFF0800502), National Natural Science Foundation of China (NSFC 41673062), and the National
660 Second Scientific Expedition to the Tibetan Plateau (2019QZKK0707). M.L. gratefully acknowledges
661 support from the U.S. Department of Energy (DOE) National Nuclear Security Administration (NNSA)
662 through the Capital/DOE Alliance Center (DE-NA0003858). The authors thank Don Porcelli and Dhilip
663 Kumar for editorial handling, and Nick Timms, Elizabeth Bell, Aaron Cavosie, and F. J. Ryerson for their
664 constructive reviews of this manuscript and older versions. The authors express thanks to the staff at
665 beamline 4W2, Beijing Synchrotron Radiation Facility, and Heavy Ion Research Facility in Lanzhou of
666 the Institute of Modern Physics, CAS. The authors thank Marty Eakin at Wayne State University for
667 providing the natural zircons.

668

669 **Author contributions:** W.L. and R.C.E. led the study. W.L. designed the experiments, analyzed the data
670 and developed the relevant equations. W.L., M.L. and R.C.E. wrote the paper. S.N., S.W., F.Z., J.N., Y.L.,
671 P.Z., J.L. and S.Q. performed the high-pressure experiments, and S.N. performed the TEM experiments.
672 L.A.B. and R.C.E. provided the samples. All the authors contributed to the interpretation of the results.

673

674 **Supplementary material:** Details of Raman and XRD data for the critical pressure, Raman data as a
675 function of alpha-dose, the mean alpha-dose accumulated before the impact in craters, the FFT analysis
676 before and after pressurization, additional XRD patterns, and the atomic scale analysis of a twinned
677 structure. Additional data can be found in Supplementary Excel files 1 and 2.

678 **References**

679

680 Bai, F., Bian, K.F., Huang, X., Wang, Z.W. and Fan, H.Y. (2019) Pressure induced nanoparticle phase behavior, property, and
681 applications. *Chemical Reviews* **119**, 7673-7717.

682 Beirau, T., Nix, W.D., Bismayer, U., Boatner, L.A., Isaacson, S.G. and Ewing, R.C. (2016) Anisotropic mechanical properties
683 of zircon and the effect of radiation damage. *Physics and Chemistry of Minerals* **43**, 627-638.

684 Cavosie, A.J., Biren, M.B., Hodges, K.V., Wartho, J.-A., Horton Jr, J.W. and Koeberl, C. (2021) Dendritic reidite from the
685 Chesapeake Bay impact horizon, Ocean Drilling Program Site 1073 (offshore northeastern USA): A fingerprint of distal
686 ejecta? *Geology* **49**, 201-205.

687 Cavosie, A.J., Erickson, T.M. and Timms, N.E. (2015) Nanoscale records of ancient shock deformation: Reidite ($ZrSiO_4$) in
688 sandstone at the Ordovician Rock Elm impact crater. *Geology* **43**, 315-318.

689 Cavosie, A.J. and Koeberl, C. (2019) Overestimation of threat from 100 Mt–class airbursts? High-pressure evidence from
690 zircon in Libyan Desert Glass. *Geology* **47**, 609-612.

691 Cavosie, A.J., Timms, N.E., Erickson, T.M., Hagerty, J.J. and Hörz, F. (2016) Transformations to granular zircon revealed:
692 Twinning, reidite, and ZrO_2 in shocked zircon from Meteor Crater (Arizona, USA). *Geology* **44**, 703-706.

693 Cavosie, A.J., Timms, N.E., Ferrière, L. and Rochette, P. (2018) FRIGN zircon—The only terrestrial mineral diagnostic of
694 high-pressure and high-temperature shock deformation. *Geology* **46**, 891-894.

695 Chakoumakos, B.C., Murakami, T., Lumpkin, G.R. and Ewing, R.C. (1987) Alpha-decay induced fracturing in zircon: The
696 transition from the crystalline to the metamict state. *Science* **236**, 1556-1559.

697 Chen, M., Yin, F., Li, X., Xie, X., Xiao, W. and Tan, D. (2013) Natural occurrence of reidite in the Xiuyan crater of China.
698 *Meteoritics and Planetary Science* **48**, 796-805.

699 Christoffersen, R., Erickson, T., Cline, C., Cintala, M. and Timms, N. (2023) The zircon-reidite shock transformation: A TEM
700 study of reidite produced at a newly established 21.2 GPa shock pressure threshold, Lunar and Planetary Science
701 Conference.

702 Cousins, V., Cavosie, A., Quintero, R. and Timms, N. (2022) Microstructural study of zircon in red impact melt rock from
703 Gosses Bluff, Australia. *LPI Contributions* **2695**, 6271.

704 Cox, M.A., Cavosie, A.J., Bland, P.A., Miljkovic, K. and Wingate, M.T.D. (2018) Microstructural dynamics of central uplifts:
705 Reidite offset by zircon twins at the Woodleigh impact structure, Australia. *Geology* **46**, 983-986.

706 Dmitriev, V.P., Rochal, S.B., Gufan, Y.M. and Toledano, P. (1988) Definition of a transcendental order parameter for
707 reconstructive phase transitions. *Physical Review Letters* **60**, 1958-1961.

708 Du, J., Devanathan, R., René Corrales, L. and Weber, W.J. (2012) First-principles calculations of the electronic structure, phase
709 transition and properties of $ZrSiO_4$ polymorphs. *Computational and Theoretical Chemistry* **987**, 62-70.

710 Eakin, M., Brownlee, S.J., Baskaran, M. and Barbero, L. (2016) Mechanisms of radon loss from zircon: Microstructural
711 controls on emanation and diffusion. *Geochimica et Cosmochimica Acta* **184**, 212-226.

712 Erickson, T., Cline, C., Jakubek, R., Cintala, M. and Timms, N. (2020a) Shock Deformation in Zircon, a Comparison of Results
713 from Shock-Reverberation and Single-Shock Experiments, Lunar and Planetary Science Conference.

714 Erickson, T.M., Kirkland, C.L., Timms, N.E., Cavosie, A.J. and Davison, T.M. (2020b) Precise radiometric age establishes
715 Yarrabubba, Western Australia, as Earth's oldest recognised meteorite impact structure. *Nature Communications* **11**, 300.

716 Erickson, T.M., Pearce, M.A., Reddy, S.M., Timms, N.E., Cavosie, A.J., Bourdet, J., Rickard, W.D.A. and Nemchin, A.A.
717 (2017) Microstructural constraints on the mechanisms of the transformation to reidite in naturally shocked zircon.
718 *Contributions to Mineralogy and Petrology* **172**, 6.

719 Ewing, R.C. (2003) Radiation effects in zircon. *Reviews in Mineralogy and Geochemistry* **53**, 387-425.

720 Ewing, R.C. (2007) Materials science: Displaced by radiation. *Nature* **445**, 161-162.

721 Ewing, R.C., Meldrum, A., Wang, L.M., Weber, W.J. and Corrales, L.R. (2003) Radiation effects in zircon. *Reviews in*

Mineralogy and Geochemistry **53**, 387-425.

Farges, F. and Calas, G. (1991) Structural analysis of radiation damage in zircon and thorite: An X-ray absorption spectroscopic study. *American Mineralogist* **76**, 60-73.

Farley, K.A., Shuster, D.L. and Ketcham, R.A. (2011) U and Th zonation in apatite observed by laser ablation ICPMS, and implications for the (U-Th)/He system. *Geochimica et Cosmochimica Acta* **75**, 4515-4530.

Farnan, I., Cho, H. and Weber, W.J. (2007) Quantification of actinide α-radiation damage in minerals and ceramics. *Nature* **445**, 190-193.

Farnan, I. and Salje, E.K.H. (2001) The degree and nature of radiation damage in zircon observed by ^{29}Si nuclear magnetic resonance. *Journal of Applied Physics* **89**, 2084-2090.

Fiske, P.S., Nellis, W.J. and Sinha, A.K. (1994) Shock-induced phase transitions of $ZrSiO_4$, reversion kinetics, and implications for terrestrial impact craters. *EOS, Transition Americian Geophysical Union* **75**, 416-417.

Geisler, T., Pidgeon, R.T., Van Bronswijk, W. and Pleysier, R. (2001) Kinetics of thermal recovery and recrystallization of partially metamict zircon : a Raman spectroscopic study. *European Journal of Mineralogy* **13**, 1163-1176.

Geisler, T., Trachenko, K., Ríos, S., Dove, M., T. and Salje, E., K. H. (2003) Impact of self-irradiation damage on the aqueous durability of zircon ($ZrSiO_4$): implications for its suitability as a nuclear waste form. *Journal of Physics: Condensed Matter* **15**, L597.

Glasmacher, U.A., Lang, M., Keppler, H., Langenhorst, F., Neumann, R., Schardt, D., Trautmann, C. and Wagner, G.A. (2006) Phase transitions in solids stimulated by simultaneous exposure to high pressure and relativistic heavy ions. *Physical Review Letters* **96**, 195701.

Glass, B.P. and Liu, S. (2001) Discovery of high-pressure $ZrSiO_4$ polymorph in naturally occurring shock-metamorphosed zircons. *Geology* **29**, 371-373.

Glass, B.P., Liu, S. and Leavens, P.B. (2002) Reidite: An impact-produced high-pressure polymorph of zircon found in marine sediments. *American Mineralogist* **87**, 562-565.

Gucsik, A., Zhang, M., Koeberl, C., Salje, E.K.H., Redfern, S.A.T. and Pruneda, J.M. (2004) Infrared and Raman spectra of $ZrSiO_4$ experimentally shocked at high pressures. *Mineralogical Magazine* **68**, 801-811.

Guenthner, W.R., Reiners, P.W., Ketcham, R.A., Nasdala, L. and Giester, G. (2013) Helium diffusion in natural zircon: Radiation damage, anisotropy, and the interpretation of zircon (U-Th)/He thermochronology. *American Journal of Science* **313**, 145-198.

Hammersley, A.P. (2016) FIT2D: A multi-purpose data reduction, analysis and visualization program. *Journal of Applied Crystallography* **49**, 646-652.

Hasebe, N., Tamura, A. and Arai, S. (2013) Zeta equivalent fission-track dating using LA-ICPMS and examples with simultaneous U-Pb dating. *Island Arc* **22**, 280-291.

Holland, H.D. and Gottfried, D. (1955) The effect of nuclear radiation on the structure of zircon. *Acta Crystallographica* **8**, 291-300.

Kelly, P.M. and Rose, L.R.F. (2002) The martensitic transformation in ceramics - its role in transformation toughening. *Progress in Materials Science* **47**, 463-557.

Kenny, G.G., Schmieder, M., Whitehouse, M.J., Nemchin, A.A., Morales, L.F., Buchner, E., Bellucci, J.J. and Snape, J.F. (2019) A new U-Pb age for shock-recrystallised zircon from the Lappajärvi impact crater, Finland, and implications for the accurate dating of impact events. *Geochimica et Cosmochimica Acta* **245**, 479-494.

Kirby, S.H. and Stern, L.A. (1993) Experimental dynamic metamorphism of mineral single crystals. *Journal of Structural Geology* **15**, 1223-1240.

Knittle, E. and Williams, Q. (1993) High-pressure Raman-spectroscopy of $ZrSiO_4$: Observation of the zircon to scheelite transition at 300 K. *American Mineralogist* **78**, 245-252.

Kowitz, A., Güldemeister, N., Schmitt, R.T., Reimold, W.U., Wünnemann, K. and Holzwarth, A. (2016) Revision and

recalibration of existing shock classifications for quartzose rocks using low-shock pressure (2.5–20 GPa) recovery experiments and mesoscale numerical modeling. *Meteoritics & Planetary Science* **51**, 1741-1761.

Kusaba, K., Syono, Y., Kikuchi, M. and Fukuoka, K. (1985) Shock behavior of zircon phase transition to scheelite structure and decomposition. *Earth and Planetary Science Letters* **72**, 433-439.

Kusaba, K., Yagi, T., Kikuchi, M. and Syono, Y. (1986) Structural considerations on the mechanism of the shock-induced zircon-scheelite transition in $ZrSiO_4$. *Journal of Physics and Chemistry of Solids* **47**, 675-679.

Kusiak, M.A., Dunkley, D.J., Wirth, R., Whitehouse, M.J., Wilde, S.A. and Marquardt, K. (2015) Metallic lead nanospheres discovered in ancient zircons. *Proceedings of the National Academy of Sciences of the United States of America* **112**, 4958-4963.

Lang, M., Zhang, F.X., Lian, J., Trautmann, C., Neumann, R. and Ewing, R.C. (2008) Irradiation-induced stabilization of zircon ($ZrSiO_4$) at high pressure. *Earth and Planetary Science Letters* **269**, 291-295.

Lang, M., Zhang, F.X., Zhang, J.M., Wang, J.W., Schuster, B., Trautmann, C., Neumann, R., Becker, U. and Ewing, R.C. (2009) Nanoscale manipulation of the properties of solids at high pressure with relativistic heavy ions. *Nature Materials* **8**, 793-797.

Leroux, H., Reimold, W.U., Koeberl, C., Hornemann, U. and Doukhan, J.C. (1999) Experimental shock deformation in zircon: A transmission electron microscopic study. *Earth and Planetary Science Letters* **169**, 291-301.

Li, W., Cheng, Y., Feng, L., Niu, J., Liu, Y., Skuratov, V.A., Zdorovets, M.V., Boatner, L.A. and Ewing, R.C. (2021) Alpha-decay induced shortening of fission tracks simulated by *in situ* ion irradiation. *Geochimica et Cosmochimica Acta* **299**, 1-14.

Li, W.X., Lang, M., Gleadow, A.J.W., Zdorovets, M.V. and Ewing, R.C. (2012) Thermal annealing of unetched fission tracks in apatite. *Earth and Planetary Science Letters* **321-322**, 121-127.

Li, W.X., Shen, Y.H., Zhou, Y.Q., Nan, S., Chen, C.H. and Ewing, R.C. (2017) *In situ* TEM observation of alpha-particle induced annealing of radiation damage in Durango apatite. *Scientific Reports* **7**, 14108.

Mao, H.K., Xu, J. and Bell, P.M. (1986) Calibration of the ruby pressure gauge to 800 kbar under quasi-hydrostatic conditions. *Journal of Geophysical Research* **91**, 4673-4676.

Mao, W.L., Mao, H.K., Eng, P.J., Trainor, T.P., Newville, M., Kao, C.C., Heinz, D.L., Shu, J.F., Meng, Y. and Hemley, R.J. (2003) Bonding changes in compressed superhard graphite. *Science* **302**, 425-427.

Marqués, M., Contreras-García, J., Flórez, M. and Recio, J.M. (2008) On the mechanism of the zircon-reidite pressure induced transformation. *Journal of Physics and Chemistry of Solids* **69**, 2277-2280.

Martell, J., Alwmark, C., Holm-Alwmark, S. and Lindgren, P. (2021) Shock deformation in zircon grains from the Mien impact structure, Sweden. *Meteoritics & Planetary Science* **56**, 362-378.

Meldrum, A., Zinkle, S.J., Boatner, L.A. and Ewing, R.C. (1998) A transient liquid-like phase in the displacement cascades of zircon, hafnon and thorite. *Nature* **395**, 56-58.

Mihailova, B., Waeselmann, N., Stangarone, C., Angel, R.J., Prencipe, M. and Alvaro, M. (2019) The pressure-induced phase transition(s) of $ZrSiO_4$: revised. *Physics and Chemistry of Minerals* **46**, 807-814.

Miro, S., Grebille, D., Chateigner, D., Pelloquin, D., Stoquert, J.P., Grob, J.J., Costantini, J.M. and Studer, F. (2005) X-ray diffraction study of damage induced by swift heavy ion irradiation in fluorapatite. *Nuclear Instruments and Methods in Physics Research Section B-Beam Interactions with Materials and Atoms* **227**, 306-318.

Murakami, T., Chakoumakos, B.C., Ewing, R.C., Lumpkin, G.R. and Weber, W.J. (1991) Alpha-decay event damage in zircon. *American Mineralogist* **76**, 1510-1532.

Nan, S., Niu, J., Liang, L., Lu, Z., Wang, Q., Zhai, P., Liu, Y., Qin, S. and Li, W. (2022) Comparison of reidite formation between zircon bulk and nanoparticles. *Journal of Physics and Chemistry of Solids* **161**, 110475.

Niu, J., Lu, Z., Nan, S., Wu, X., Qin, S., Liu, Y. and Li, W. (2023) Phase transition of hafnon, $HfSiO_4$, at high pressure. *Journal of the American Ceramic Society* **106**, 6292-6300.

Ono, S., Funakoshi, K., Nakajima, Y., Tange, Y. and Katsura, T. (2004) Phase transition of zircon at high P-T conditions. *Contributions to Mineralogy and Petrology* **147**, 505-509.

Özkan, H. (2008) Effect of nuclear radiation on the elastic moduli of zircon. *Journal of Applied Physics* **47**, 4772-4779.

Pidgeon, R.T., Oneil, J.R. and Silver, L.T. (1966) Uranium and lead isotopic stability in a metamict zircon under experimental hydrothermal conditions. *Science* **154**, 1538-1540.

Plan, A., Kenny, G.G., Erickson, T.M., Lindgren, P., Alwmark, C., Holm-Alwmark, S., Lambert, P., Scherstén, A. and Söderlund, U. (2021) Exceptional preservation of reidite in the Rochechouart impact structure, France: New insights into shock deformation and phase transition of zircon. *Meteoritics & Planetary Science* **56**, 1795-1828.

Reddy, S.M., van Riessen, A., Saxey, D.W., Johnson, T.E., Rickard, W.D.A., Fougerouse, D., Fischer, S., Prosa, T.J., Rice, K.P., Reinhard, D.A., Chen, Y. and Olson, D. (2016) Mechanisms of deformation-induced trace element migration in zircon resolved by atom probe and correlative microscopy. *Geochimica et Cosmochimica Acta* **195**, 158-170.

Reid, A.F., & Ringwood, A. E. (1969) Newly observed high pressure transformations in Mn_3O_4, $CaAl_2O_4$, and $ZrSiO_4$. *Earth and Planetary Science Letters* **6**, 205-208.

Rios, S., Salje, E.K.H., Zhang, M. and Ewing, R.C. (2000) Amorphization in zircon: evidence for direct impact damage. *Journal of Physics-Condensed Matter* **12**, 2401-2412.

Rodríguez-Carvajal, J. (2001) Recent developments of the program FULLPROF. *Commission on Powder Diffraction (IUCr). Newsletter* **26**, 12-19.

Schmieder, M. and Kring, D.A. (2020) Earth's impact events through geologic time: A list of recommended ages for terrestrial impact structures and deposits. *Astrobiology* **20**, 91-141.

Shuster, D.L., Flowers, R.M. and Farley, K.A. (2006) The influence of natural radiation damage on helium diffusion kinetics in apatite. *Earth and Planetary Science Letters* **249**, 148-161.

Stangarone, C., Angel, R.J., Prencipe, M., Mihailova, B. and Alvaro, M. (2019) New insights into the zircon-reidite phase transition. *American Mineralogist* **104**, 830-837.

Timms, N.E., Erickson, T.M., Pearce, M.A., Cavosie, A.J., Schmieder, M., Tohver, E., Reddy, S.M., Zanetti, M.R., Nemchin, A.A. and Wittmann, A. (2017) A pressure-temperature phase diagram for zircon at extreme conditions. *Earth-Science Reviews* **165**, 185-202.

Timms, N.E., Healy, D., Erickson, T.M., Nemchin, A.A. and Cavosie, A.J. (2018) Role of elastic anisotropy in the development of deformation microstructures in zircon, in: Moser, D.E., Corfu, F., Darling, J.R., Reddy, S., Tait, K.T. (Eds.), Microstructural geochronology: planetary records down to atom scale: New Jersey, USA, John Wiley & Sons, American Geophysical Union Geophysical Monograph, pp. 183-202.

Tolometti, G.D., Erickson, T.M., Osinski, G.R., Cayron, C. and Neish, C. (2022) Hot rocks: Constraining the thermal conditions of the Mistastin Lake impact melt deposits using zircon grain microstructures. *Earth and Planetary Science Letters* **584**, 117523.

Tracy, C.L., Lang, M., Pray, J.M., Zhang, F.X., Popov, D., Park, C.Y., Trautmann, C., Bender, M., Severin, D., Skuratov, V.A. and Ewing, R.C. (2015) Redox response of actinide materials to highly ionizing radiation. *Nature Communications* **6**, 6133.

Utsunomiya, S., Valley, J.W., Cavosie, A.J., Wilde, S.A. and Ewing, R.C. (2007) Radiation damage and alteration of zircon from a 3.3 Ga porphyritic granite from the Jack Hills, Western Australia. *Chemical Geology* **236**, 92-111.

Valley, J.W., Cavosie, A.J., Ushikubo, T., Reinhard, D.A., Lawrence, D.F., Larson, D.J., Clifton, P.H., Kelly, T.F., Wilde, S.A., Moser, D.E. and Spicuzza, M.J. (2014) Hadean age for a post-magma-ocean zircon confirmed by atom-probe tomography. *Nature Geoscience* **7**, 219-223.

van Westrenen, W., Frank, M.R., Hanchar, J.M., Fei, Y.W., Finch, R.J. and Zha, C.S. (2004) *In situ* determination of the compressibility of synthetic pure zircon ($ZrSiO_4$) and the onset of the zircon-reidite phase transition. *American Mineralogist* **89**, 197-203.

Vetter, J., Scholz, R., Dobrev, D. and Nistor, L. (1998) HREM investigation of latent tracks in GeS and mica induced by high energy ions. *Nuclear Instruments and Methods in Physics Research Section B-Beam Interactions with Materials and Atoms* **141**, 747-752.

Walton, E.L., Timms, N.E., Hauck, T.E., MacLagan, E.A. and Herd, C.D.K. (2019) Evidence of impact melting and post-impact decomposition of sedimentary target rocks from the Steen River impact structure, Alberta, Canada. *Earth and Planetary Science Letters* **515**, 173-186.

Weber, W.J., Ewing, R.C. and Meldrum, A. (1997) The kinetics of alpha-decay-induced amorphization in zircon and apatite containing weapons-grade plutonium or other actinides. *Journal of Nuclear Materials* **250**, 147-155.

Wittmann, A., Cavosie, A.J., Timms, N.E., Ferrière, L., Rae, A., Rasmussen, C., Ross, C., Stockli, D., Schmieder, M. and Kring, D.A. (2021) Shock impedance amplified impact deformation of zircon in granitic rocks from the Chicxulub impact crater. *Earth and Planetary Science Letters* **575**, 117201.

Wittmann, A., Kenkmann, T., Schmitt, R.T. and Stöffler, D. (2006) Shock-metamorphosed zircon in terrestrial impact craters. *Meteoritics and Planetary Science* **41**, 433-454.

Woodhead, J.A., Rossman, G.R. and Silver, L.T. (1991) The metamictization of zircon: Radiation dose-dependent structural characteristics. *American Mineralogist* **76**, 74-82.

Xing, W., Lin, Y., Zhang, C., Zhang, M., Hu, S., Hofmann, B.A., Sekine, T., Xiao, L. and Gu, L. (2020) Discovery of reidite in the lunar meteorite Sayh al Uhaymir 169. *Geophysical Research Letters* **47**, e2020GL089583.

Yue, B.B., Hong, F., Merkel, S., Tan, D.Y., Yan, J.Y., Chen, B. and Mao, H.K. (2016) Deformation behavior across the zircon-scheelite phase transition. *Physical Review Letters* **117**, 135701.

Zhang, F., Tong, Y., Xue, H., Keum, J.K., Zhang, Y., Boulle, A., Debelle, A. and Weber, W.J. (2019) Strain engineering 4H-SiC with ion beams. *Applied Physics Letters* **114**, 221904.

Zhang, F.X., Wang, J.W., Lian, J., Lang, M.K., Becker, U. and Ewing, R.C. (2008) Phase stability and pressure dependence of defect formation in $Gd_2Ti_2O_7$ and $Gd_2Zr_2O_7$ pyrochlores. *Physical Review Letters* **100**, 045503.

Zhang, F.X., Xue, H.Z., Keum, J.K., Boulle, A., Zhang, Y.W. and Weber, W.J. (2020) Symmetry degeneration and room temperature ferroelectricity in ion-irradiated $SrTiO_3$. *Journal of Physics: Condensed Matter* **32**, 355405.

Zhang, M., Salje, E.K.H., Farnan, I., Graemebarber, A., Daniel, P., Ewing, R.C., Clark, A.M. and Leroux, H. (2000) Metamictization of zircon: Raman spectroscopic study. *Journal of Physics: Condensed Matter* **12**, 1915-1925.

Zhao, J., Xiao, L., Xiao, Z., Morgan, J.V., Osinski, G.R., Neal, C.R., Gulick, S.P., Riller, U., Claeys, P. and Zhao, S. (2021) Shock-deformed zircon from the Chicxulub impact crater and implications for cratering process. *Geology* **49**, 755-760.